

Article

Real-Time Measurement of Atmospheric CO₂, CH₄ and N₂O above Rice Fields Based on Laser Heterodyne Radiometers (LHR)

Jun Li ^{1,2,†}, Zhengyue Xue ^{1,3,†} , Yue Li ^{1,2}, Guangyu Bo ², Fengjiao Shen ³, Xiaoming Gao ^{1,2}, Jian Zhang ^{4,5,*}  and Tu Tan ^{2,*}

¹ School of Environmental Science and Optoelectronic Technology, University of Science and Technology of China, Hefei 230031, China

² Anhui Institute of Optics and Fine Mechanics, Chinese Academy of Sciences, Hefei 230031, China

³ School of Advanced Manufacturing Engineering, Hefei University, Hefei 230601, China

⁴ Faculty of Agronomy, Jilin Agricultural University, Changchun 130108, China

⁵ Department of Biology, University of Columbia Okanagan, Kelowna, BC V1V 1V7, Canada

* Correspondence: jian.zhang@ubc.ca (J.Z.); tantu@aiofm.ac.cn (T.T.)

† These authors contributed equally to this work.

Abstract: High-precision observations provide an efficient way to calculate greenhouse gas emissions from agricultural fields and their spatial and temporal distributions. Two high-resolution laser heterodyne radiometers (LHRs) were deployed in the suburb of Hefei (31.9°N 117.16°E) for the remote sensing of atmospheric CO₂, CH₄ and N₂O above rice paddy fields. The atmospheric transmittance spectra of CO₂, CH₄ and N₂O were measured simultaneously in real time, and the atmospheric total column abundance was retrieved from the measured data based on the optimal estimation algorithm, with errors of 0.7 ppm, 4 ppb and 2 ppb, respectively. From July to October, the abundance of CO₂ in the atmospheric column that was influenced by emissions from rice fields increased by 0.7 ppm CH₄ by 30 ppb, and by 4 ppb N₂O. During the rice growth season, rice paddy fields play a role in carbon sequestration. CH₄ and N₂O emissions from paddy fields are negatively correlated. The method of baking rice paddy fields reduces CH₄ emissions from rice fields, but N₂O emissions from rice fields are usually subsequently increased. The measurement results showed that LHRs are highly accurate in monitoring atmospheric concentrations and have promising applications in monitoring emissions from rice paddy fields. In the observation period, rice paddy fields can sequester carbon, and CH₄ and N₂O emissions from rice fields are negatively correlated. The LHRs have strong application prospects for monitoring emissions from agricultural fields.

Keywords: laser heterodyne radiometer; carbon dioxide; methane; nitrous oxide; field measurement



Citation: Li, J.; Xue, Z.; Li, Y.; Bo, G.; Shen, F.; Gao, X.; Zhang, J.; Tan, T. Real-Time Measurement of Atmospheric CO₂, CH₄ and N₂O above Rice Fields Based on Laser Heterodyne Radiometers (LHR). *Agronomy* **2023**, *13*, 373. <https://doi.org/10.3390/agronomy13020373>

Academic Editor: Wei Zhang

Received: 14 December 2022

Revised: 9 January 2023

Accepted: 26 January 2023

Published: 27 January 2023



Copyright: © 2023 by the authors. Licensee MDPI, Basel, Switzerland. This article is an open access article distributed under the terms and conditions of the Creative Commons Attribution (CC BY) license (<https://creativecommons.org/licenses/by/4.0/>).

1. Introduction

Carbon dioxide (CO₂), methane (CH₄) and nitrous oxide (N₂O) are the three most important anthropogenic greenhouse gases (GHGs) in the atmosphere and play a role in global warming [1–3]. CO₂ has a lifetime in the atmosphere for several decades to a century [4]. The concentration of CO₂ in the atmosphere has increased from 178 parts per million (ppm) to 420 ppm since the Industrial Revolution, and has increased by 3 ppm per year in recent years. CH₄ and N₂O are classified as important greenhouse gases other than CO₂. The changes in CH₄ and N₂O concentrations are considered as critical factors that influence the atmospheric greenhouse effect. The lifetime of CH₄ in the atmosphere is about 12 years, and the global average total column abundance of CH₄ in 2020 was 1920 parts per billion (ppb). N₂O has a lifetime of 114 years, and the global average total column abundance of N₂O was about 340 ppb in 2020. Within 100 years, the warming potentials of CH₄ and N₂O will be 25 and 300 times higher than those of CO₂, respectively [5,6]. Moreover, nitric oxide (NO), the product of N₂O photolysis which occurs in the stratosphere,

depletes stratospheric ozone and leads to the destruction of the structure of the ozone layer. From 1990 to 2019, global agricultural GHG emissions increased by 17%. Agroforestry sources account for 22% of total global greenhouse gas emissions, whereas agricultural sources account for 14% of total global greenhouse gas emissions. Rice fields are considered one of the major sources of greenhouse gas emissions in agroecosystems [7]. Under climate, vegetation, soil and anthropogenic disturbance, the organic matter of farmland soil is decomposed by microorganisms into inorganic carbon and nitrogen, and the inorganic carbon is mostly released into the atmosphere as CO₂ under aerobic conditions and as CH₄ under anaerobic conditions. Nitrogen is converted to nitrate nitrogen by nitrifying bacteria, nitrate nitrogen is converted to various states of nitrogen oxides by denitrifying bacteria and N₂O is produced during both nitrification and denitrification. More than half of global N₂O is the product of nitrification and denitrification in soils [8]. China is a large rice growing country, with the second largest rice growing area in the world and great potential to achieve high yields and low emissions. Reducing GHG emissions from rice fields requires not only innovative rice management practices, but also accurate estimates of GHG emissions from rice fields and research on the spatial and temporal characteristics of greenhouse gas emissions. Monitoring the production, emission and transport of GHGs during rice production can help to assess the effectiveness of interventions to reduce emissions in rice production, and achieve a balance between abundant rice production and GHG emission reduction. It would provide assistance to promoting the green transformation of agricultural production as well [7].

The observation of greenhouse gas emissions from agricultural fields is mainly based on static chamber gas chromatography, which has long measurement intervals and makes it difficult to achieve real-time continuous measurements. Moreover, the eddy covariance technique obtains emission fluxes from agricultural fields by measuring the covariance of temperature, target gas concentration and vertical wind speed, which has the advantages of wide applicability and high reliability [9]. Gu et al. reported on a sensor based on the eddy covariance technique, which was designed to measure CO₂ and H₂O flux emissions at Jiangdu Agricultural Monitoring Station in Jiangsu Province [10]. In situ field observations of greenhouse gas emission fluxes from rice fields are scarce, and the simultaneous monitoring of CO₂, CH₄ and N₂O emission fluxes from rice fields is still lagging. Emission flux data measured in the field in some localized areas cannot be reliably extrapolated to regional and global scales and are not available for studying the spatial and temporal characteristics of GHG emissions from agricultural sources. High-precision observations of regional atmospheric GHG concentrations provide an effective way to calculate greenhouse gas emissions in large-scale rice paddy fields and their spatial and temporal distribution [11]. The successive measurement of atmospheric GHG column abundances over rice fields and the calculation of daily average column abundance changes can effectively monitor emissions of any given size rice field. LHR is a passive atmospheric gas remote sensing sensor that is portable, compact and has low power consumption and high sensitivity, which means that LHR could be easily deployed for long-term accurate greenhouse gas emission monitoring of rice field areas [12]. Since it was first applied to the detection of O₃ column concentration in the 1970s, it has been widely used in the measurement of vertical profiles and column concentrations of atmospheric greenhouse gases [13,14]. In recent years, LHR system integration has greatly improved with the development of low-cost lasers, waveguides and fiber technology and its application products. Wilson and co-workers [15] and Wang et al. [16] developed near infrared (NIR) LHR for the measurements of atmospheric vertical profiles of CO₂ and CH₄. Wang used the developed NIR LHR to measure CO₂ and CH₄ column concentrations in Hefei over a 6-month period, where the column abundance variation was mainly due to vehicle emissions. Weidmann et al. [17,18] and Xue [19] developed mid infrared (MIR) LHR using an inter-band cascade laser (ICL) as the local oscillator (LO) for the measurements of atmospheric column abundance of CH₄, N₂O and H₂O.

In this paper, high-precision and portable greenhouse gas measurement sensors NIR LHR and MIR LHR were developed in the laboratory and deployed in the suburbs of Hefei (31.9°N 117.16°E) to effectively monitor greenhouse gas emissions during the growth of rice. In the NIR LHR, two distributed feedback (DFB) lasers centered at 1.603 μm and 1.65 μm were used as LOs for CO_2 and CH_4 observations. In the two MIR LHR, inter-band cascade lasers centered at 3.53 μm and 3.93 μm were used as LOs for N_2O and CH_4 observations. The high-resolution atmospheric transmittance spectra of CO_2 , CH_4 and N_2O were measured simultaneously, and the real-time column abundance was retrieved. The variation trend of atmospheric column concentration of three gases from July to October of 2022 was analyzed in combination with the planting change in the surrounding farmland. Based on the long-term real-time observation data, the effectiveness of rice production emission reduction interventions is evaluated and reported here. The specific experimental device, measurement and inversion results and data analysis will be presented later.

2. Materials and Methods

LHR, whether near-infrared (NIR) or mid-infrared (MIR) LHR, which extracts atmospheric molecular absorption information from sunlight via beating with a local oscillator (LO) on a photodetector, has been successfully applied to the remote sensing of the atmosphere in recent years [20]. The basic principle of LHR has been explained in detail in reference [1]. Here, the schematic diagram of LHR is shown in Figure 1a. Sunlight containing molecular absorption information is captured by a high-precision sun tracker. Then, almost perfectly aligned chop-modulated sunlight and LO are incident on the photodetector (PD). Molecular absorption information is transferred to the radio frequency (RF) component of the response current of the photodetector. The mean-square detector (M-S PD) converts the RF current into low-frequency voltage, and the atmospheric molecular absorption spectrum is obtained by demodulating the low-frequency voltage signal using a lock-in amplifier (LIA). It is worth noting that the resolution and the instrument line shape (ILS) of the LHR are determined by the electrical bandwidth of the filter, which allows for high spectral resolution. Atmospheric transmission spectra with a high resolution and signal-to-noise ratio will help with obtaining accurate atmospheric column abundances. A personal computer (PC) and high sampling rate data acquisition (DAQ) card serve for instrument control, data acquisition and processing.

The observation equipment used were laboratory-made highly integrated portable NIR and MIR LHR systems as shown in Figure 1b. The NIR LHR system was mainly composed of an all-fiber NIR LHR and an optical fiber sun tracker. In the all-fiber NIR LHR, two distributed feedback (DFB) lasers centered at 1.603 μm and 1.65 μm were used for CO_2 detection with a spectral resolution of 0.013 cm^{-1} , and for CH_4 detection one with a spectral resolution of 0.0067 cm^{-1} was used, respectively. The tracking precision of the fiber-optic solar tracker was 4×10^{-3} mrad, which is far smaller than the divergence angle of sunlight (9.6×10^{-3} rad). The alignment between the sunlight and LO was achieved by using the single-mode fiber coupler. The MIR LHR system was mainly composed of a free space solar tracker and a micro-electro-mechanical system (MEMS) modulator-based dual-channel MIR LHR. In this LHR, two inter-band cascade lasers (ICLs) centered at 3.53 μm and 3.93 μm were used as the LOs to probe the absorption lines of CH_4 with a resolution of 0.0047 cm^{-1} and of N_2O with a resolution of 0.0053 cm^{-1} , respectively. The two LHRs worked in the ground-based solar occultation mode. For the purpose of atmospheric molecular transmission spectrum detection, the laser wavenumber covered the molecular absorption range of interest by tuning the laser injection current at a fixed operating temperature. Both LHRs had CH_4 detection channels, which allowed for the validation of the accuracy of inversion results. Moreover, the reliability of the instrument and inversion algorithm have been effectively evaluated in previous work [16,20].

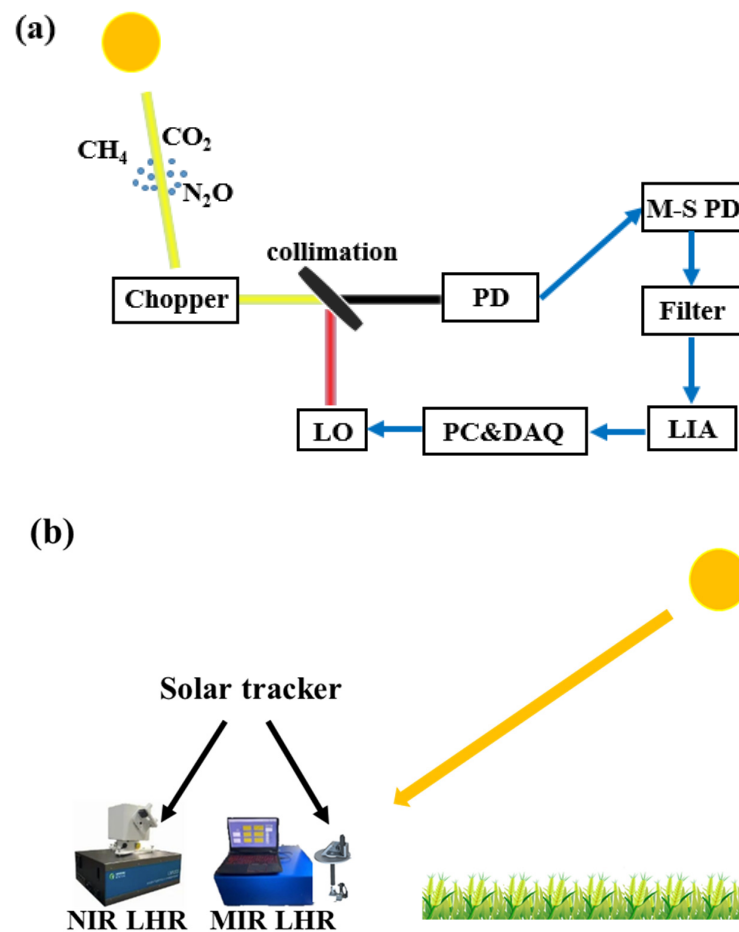


Figure 1. (a) Schematic diagram of LHR. LO: local oscillator, PD: photodetector, M-S PD: mean-square photodetector, LIA: lock-in amplifier, DAQ: data acquisition, PC: personal computer; (b) photo of the near-infrared laser heterodyne radiometer (NIR LHR) and mid-infrared laser heterodyne radiometer (MIR LHR).

The two LHRs were deployed in a suburb of Hefei (31.9°N 117.16°E) for atmospheric total column measurement of GHGs. In this work, the LO center frequency was scanned to probe the absorption line of (6238.77 cm^{-1}), CH_4 (at 6036.65 cm^{-1} and at 2831.92 cm^{-1}) and N_2O (at 2538.34 cm^{-1}). In order to obtain a high signal-to-noise (SNR) ratio atmospheric transmittance spectrum, a typical scan time was about 8 min. The observation period was from 1 July to 15 October 2022, which is basically consistent with the planting time of late season rice.

3. Results

The examples of atmospheric CO_2 (Figure 2a and CH_4 : Figure 2b) transmittance spectra measured by NIR LHR are presented, and the SNR of CO_2 signal and CH_4 signal are 180 and 200, respectively.

The MIR-LHR measurement results of $3.53\text{ }\mu\text{m}$ (CH_4) and $3.93\text{ }\mu\text{m}$ (N_2O) detection channels are shown in Figure 3a (red curve) and Figure 3b (blue curve). The SNR of $3.53\text{ }\mu\text{m}$ and $3.93\text{ }\mu\text{m}$ detection channels are 70 and 90, respectively. The atmospheric transmittance spectrum of CH_4 is deformed, mainly affected by the water isotope (HDO) absorption. The measured atmospheric transmittance spectrum of HDO offers an efficient path to research the atmospheric total column abundance of water vapor, which will be the emphasis of future work. Compared with NIR LHR, the SNR of the CH_4 detection channel signal of the MIR LHR is significantly lower, which leads to large measurement errors [21–23].

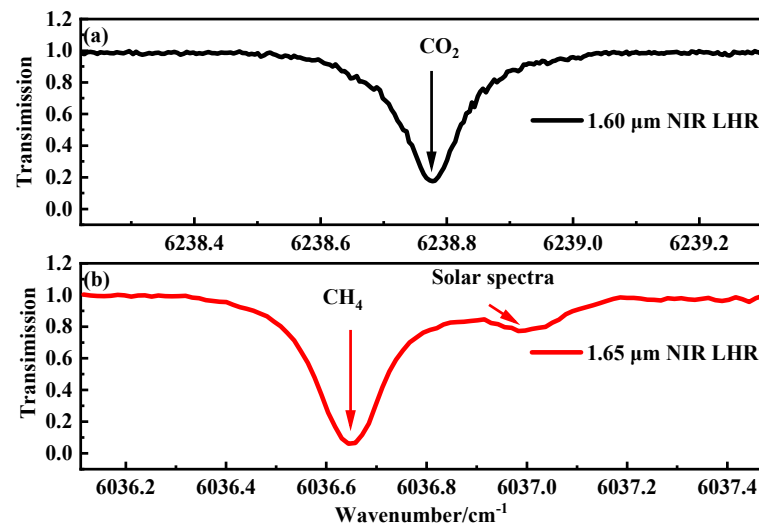


Figure 2. Atmospheric transmittance spectra measured by NIR LHR. (a) CO₂ at 6238.77 cm⁻¹; (b) CH₄ at 6036.65 cm⁻¹.

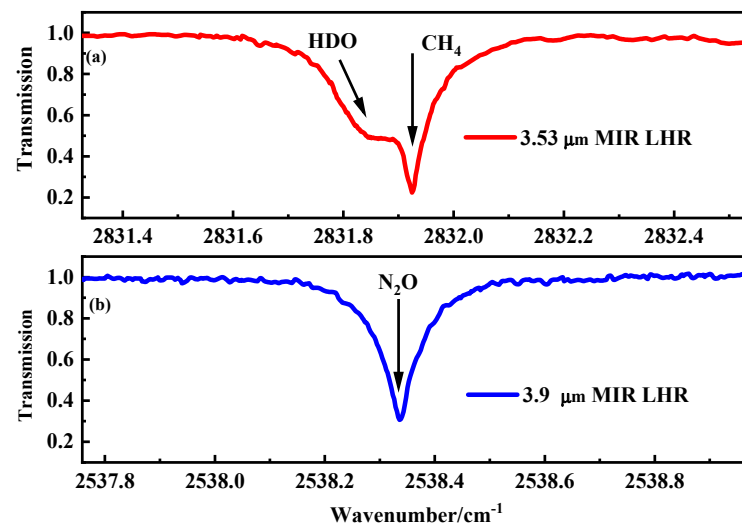


Figure 3. Atmospheric transmittance spectra measured by MIR LHR. (a) CH₄ at 2831.92 cm⁻¹; (b) N₂O at 2538.34 cm⁻¹.

LHR data retrieval was performed using the optimal estimation method (OEM), which was proposed by Rodgers for atmospheric remote sensing retrieval. Weidmann et al. gave a detailed introduction to the application of OEM in LHR data retrieval [24]. Herein, a brief recall is presented. The radiative transfer forward model (F) based on the reference forward model (RFM) was used to calculate the atmospheric transmittance spectrum of the solar radiance, which represents the absorption of solar radiation by greenhouse gases emitted from rice fields and by greenhouse gases in the atmosphere [25]. The relationship between the LHR data and the atmospheric state vector is described as:

$$y_m = F(x_n) + \varepsilon \quad (1)$$

where y_m is the measurement vector, x_n is the state vector including the temperature (T), pressure (P) and volume mixing ratio (VMR) and ε is the error vector. The OEM-based data retrieval is an iterative process to minimize the cost function (χ^2):

$$\chi^2 = (y_m - F(x_n))S_\varepsilon^{-1}(y_m - F(x_n))^T + (x_a - x_n)S_a^{-1}(x_a - x_n)^T \quad (2)$$

where S_ε is the measurement covariance matrix, S_a is the prior covariance matrix and x_a is the prior state. The Levenberg–Marquardt (LM) method was adopted in the iterative process. The iterative state vector x_{i+1} was calculated using Equation (3).

$$x_{i+1} = x_i + \left((1 + \gamma)S_a^{-1} + K_i^T S_\varepsilon^{-1} K_i \right)^{-1} \times \left[K_i^T S_\varepsilon^{-1} (y_m - F_i) - S_a^{-1} (x_i - x_a) \right] \quad (3)$$

where K is the weighting function and γ is the LM parameter.

The flow-chart of LHR retrieval is displayed in Figure 4, which consists of a forward model and an inversion program. In the forward calculation, the atmospheric transmission spectrum ($F(x_n)$) combined with the corresponding weighting function (K) are calculated with the input atmospheric parameters (temperature (T), pressure (P) and volume mixing ratios (VMRs)), ILS , a priori state vector and solar zenith angle. In the inverse program, the forward model is iteratively called to minimize the cost function (Eq. (2)) following the LM algorithm (Eq. (3)); finally, the profile of the target gas is obtained. According to the retrieved profile, the atmospheric total column abundance of CO_2 is calculated to be ~ 428 ppm, the atmospheric total column abundance of CH_4 is found to be ~ 1940 ppb (NIR LHR) and ~ 1939 ppb (MIR LHR), and the atmospheric total column abundance of N_2O is found to be ~ 335 ppm, respectively. The detection accuracy of the LHRs is mainly affected by the error caused by the system noise and the retrieval error. Improving the signal-to-noise ratio of LHRs' signal and employing more accurate a priori data will improve measurement accuracy. In this study, considering the measurement error and retrieval error, the total errors are calculated to be $\sim 0.2\%$ (CO_2), $\sim 0.23\%$ (NIR LHR, CH_4), $\sim 1\%$ (MIR LHR, CH_4) and $\sim 0.8\%$ (N_2O), respectively.

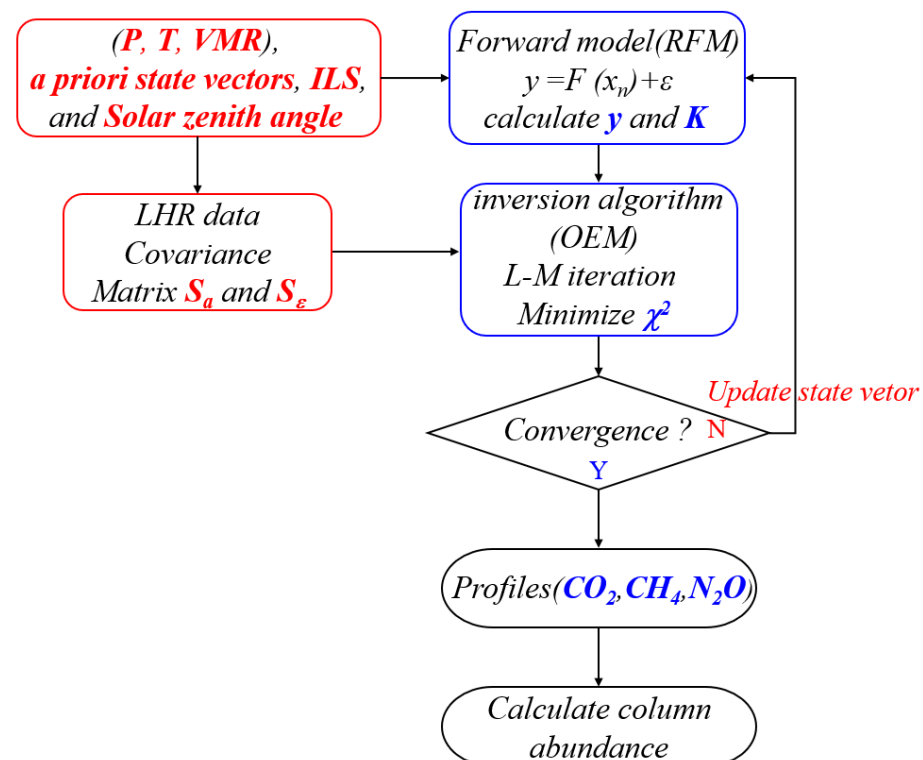


Figure 4. Flow-chart of the LHR retrieval.

4. Discussion

The farmland in the suburb of Hefei (31.9°N 117.16°E) is mainly planted with late season rice, and the planting period of late season rice is from mid-early June to mid-early October. Therefore, our observation period was from 1 July to 15 October 2022. It should be noted that LHRs extract information from solar radiation; therefore, only the results

measured on a clear, cloudless day were analyzed in this study. In addition, compared to the conventional indoor gas chromatography and eddy covariance techniques, the LHRs measure the total column abundance in the atmospheric column; they cannot measure the flux in the rice field. Since there are no other influential emission sources around the rice fields, the column abundance variation during the measurement period represents the total emission of a rice paddy area. A comprehensive understanding of the emission patterns of CO₂, CH₄ and N₂O and their interrelationships is a prerequisite and plays a key role in achieving greenhouse gas emission reduction in rice fields. In order to focus on the relationship between the emission in rice paddy fields and atmospheric column abundance of CO₂, CH₄ and N₂O, data measured from 1 July to 15 October 2022 are used to analyze the variation trend of atmospheric CO₂, CH₄ and N₂O column concentrations above paddy fields.

4.1. Atmospheric CO₂

To understand the trend of CO₂ emission from rice fields during daytime, we measured CO₂ concentration over rice fields from 10:00 a.m. to 15:00 p.m. on 1 July, 1 September, and 15 October 2022, and the measurement results are shown in Figure 5a. The high fluctuations in the total column abundance of CO₂ measured at 10:00–11:00 are probably due to the instability of atmospheric parameters (e.g., temperature and pressure) during this time period. Therefore, the daily average total column abundance mentioned in this manuscript was calculated from data measured after 11:00 on the day. During each day of measurement, the total column abundance of atmospheric CO₂ tends to decrease, which is mainly influenced by the consumption of atmospheric CO₂ via the photosynthesis of plants, such as rice.

The daily average total column abundance of CO₂ in the atmosphere above the rice paddy fields in the suburbs of Hefei from July to mid-October is shown in Figure 5b, where the gray shaded part indicates that the weather condition was cloudy or rainy on that day. The average monthly column abundance of CO₂ in July, August, September and October was 427.2, 427.4, 427.8 and 428.1 ppm, respectively. The standard deviations of total column abundance of CO₂ are calculated to be in the range of 0.6–1.4 ppm, which corresponds to an uncertainty region of 0.21–0.46%. The atmospheric total column abundance of CO₂ increased, but the growth rate of CO₂ concentration was less than the expectation reported by IPCC [8]. It can be inferred that the rice paddy field plays a certain role in carbon sequestration during the rice growing season. An increase in CO₂ emission from rice fields during the baking period and a decrease in soil CO₂ emission rate with decreasing temperature were not observed. The possible reasons for this are the lack of measurement accuracy of LHRs, the inability of the LHRs to make accurate measurements of the ground surface and atmospheric circulation.

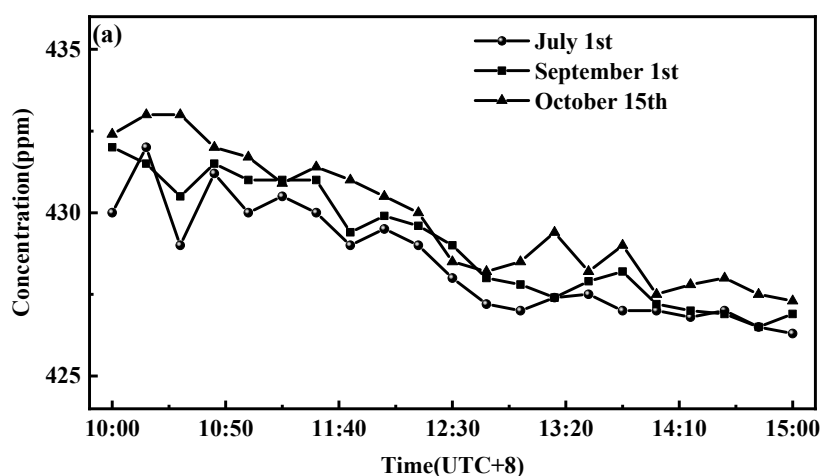


Figure 5. Cont.

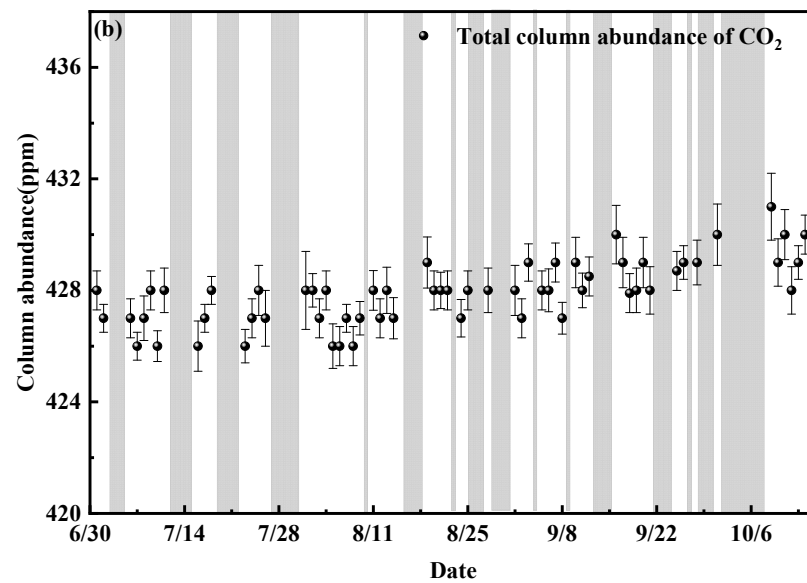


Figure 5. Total column abundance of CO₂. (a) Retrieval results of CO₂ from 10:00 am to 15:00 pm on 1 July, 1 September and 15 October 2022; (b) time series of the CO₂ retrieval results. Estimations of 95% confidence ranges are indicated.

4.2. Atmospheric CH₄

The average CH₄ emission flux of late season rice was much higher than that of early season rice. Emission fluxes from rice fields with late rice growth were greater than those with early rice growth. CH₄ emissions from rice fields were mainly concentrated in the tillering stage of rice growth (about late August to September), and decreased in the middle and late stages of rice growth, especially after baking, and slightly increased after rice fields were re-watered [26]. After that, the paddy field maintained low emissions until the rice harvest. The retrieval results of CH₄ above rice paddy fields in the suburbs of Hefei are shown in Figure 6, where the atmospheric column abundance of CH₄ increased from July and its high value appeared at the end of August. The standard deviations are found to be in the range of 5–12 ppb for the total column abundance of CH₄, which corresponds to an uncertainty region of 0.18–0.5%. During the rice growing season, the total atmospheric column abundance of CH₄ above the rice fields increased by 30 ppb. From early July to the end of August when rainfall is abundant and rice fields are in a flooded state, inorganic carbon is released into the atmosphere as CH₄ in the absence of oxygen. In addition, the increase in soil temperature promotes the production and emission of CH₄. Despite the presence of more rainy days in September and October, the methane concentration decreased significantly due to baked fields and lower temperatures. The CH₄ column concentration decreased from mid-September due to the gradual diffusive mixing of atmospheric CH₄ from the lower to middle layers and the horizontal atmospheric motion. CH₄ emissions from rice fields decline after October as rice has been harvested. During the non-rice growing season, CH₄ column concentrations over rice fields will slowly increase due to other anthropogenic sources such as fossil fuel and landfill emissions.

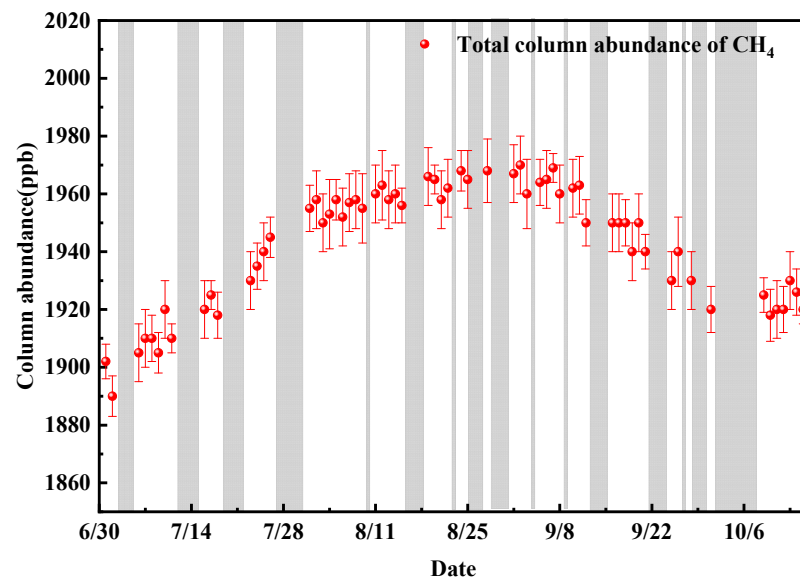


Figure 6. Time series of the CH₄ retrieval results. Estimations of 95% confidence ranges are indicated.

4.3. Atmospheric N₂O

The production and emission of N₂O in rice paddy fields are affected by soil temperature, humidity and PH. The relevant research shows that rice plants are the main channel for N₂O transmission. The atmospheric total column abundance of N₂O with a wave-like trend from July to mid-October above rice paddy fields around Hefei is displayed in Figure 7. The standard deviation of the N₂O total column is between 2 and 4 ppb with a corresponding uncertainty range of 0.3–0.8%. The purple shaded part indicates that there was a thunderstorm shower on that day. The dates were 4, 5, 28, 30 July and 14 September. Affected by paddy irrigation, N₂O emissions from paddy fields decreased. The total column abundance of atmospheric N₂O gradually decreased from July. The atmospheric column abundance of N₂O increased from the end of July to early August and in September. During this period, the paddy field changed from flooding to drying, and the soil redox potential increased, which was conducive to the conversion of ammonia to N₂O and greatly promoted the emission of N₂O. In early October, nitrification was inhibited by strong cold air and precipitation, which led to a decrease in N₂O emissions from paddy fields. As rice is harvested, although bare farmland is a weak N₂O source, it can be predicted that atmospheric N₂O total column abundance will decrease further in late October; after that, the variation in atmospheric N₂O concentration will no longer be dominated by farmland emissions. It is worth noting that when lightning occurs, nitrogen and oxygen in the air will form nitric acid through an ionization reaction and chemical reaction, reducing the PH of the soil, which will improve the efficiency of nitrification and promote the formation of N₂O. However, significant variation in atmospheric N₂O column abundance is not observed in Figure 3. On the one hand, several consecutive days' precipitation before and after the thunderstorm (28 July, 30 July) inhibits the nitrification in the soil. On the other hand, the retrieval results, which are limited by the measurement accuracy of the MIR LHR, cannot reflect the weak variation in atmospheric N₂O column abundance.

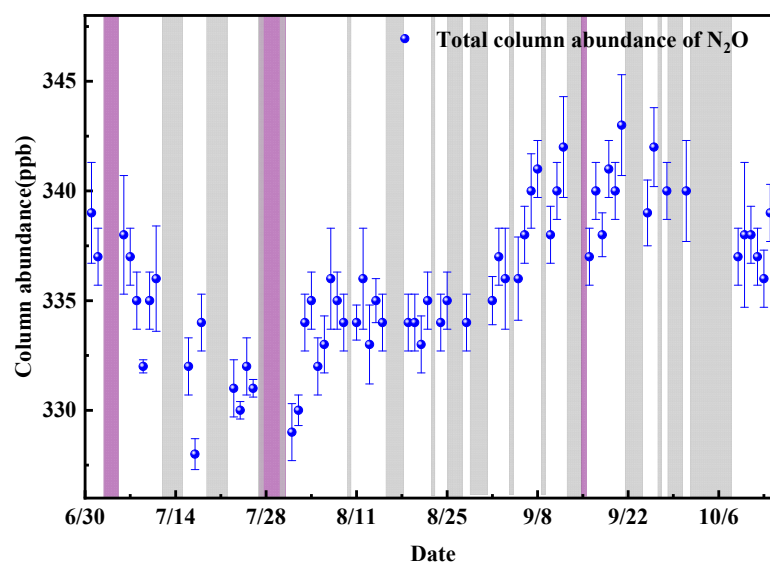


Figure 7. Time series of the N_2O retrieval results. Estimations of 95% confidence ranges are indicated.

As shown in Figures 5–7, there was no significant correlation between CO_2 and CH_4 emissions throughout the rice growing season. The emission patterns of CH_4 and N_2O in rice fields, especially the peak emission period, were mainly influenced by the moisture and soil temperature of rice fields, and the emissions of CH_4 and N_2O in rice fields were negatively correlated. The relationship between CH_4 and N_2O emissions in paddy fields is mainly shown by irrigation management and the amount of nitrogen fertilizer applied. Field drying and water-saving irrigation are key tools used to reduce CH_4 emissions from rice fields. The mid-term baking of paddy fields decreases CH_4 emissions while inevitably increasing N_2O emissions. Therefore, the appropriate timing of field baking is critical and the reduction effect should be assessed in terms of combined CH_4 and N_2O warming potential. The optimization of fertilizer management and the adjustment of the ratio of fertilizer nitrogen to potassium to phosphorus can help to control N_2O emissions from rice fields. During the rice growing period, a combination of soil properties, tillage practices, temperature and humidity are considered to maximize the reduction effect. We suggest that rice varieties with less greenhouse gas emissions should be promoted in rice seed selection, and rice fields should be kept as dry as possible to reduce CH_4 emissions during the early rice growth period, and shallow irrigation with chemical fertilizers should be used to suppress N_2O emissions during the late rice growth period. Considering the year-round CH_4 and N_2O emissions from rice fields, water management of rice fields and emission monitoring of paddy fields should not be neglected during the non-rice growing period.

5. Conclusions

In this study, NIR LHR and MIR LHR were deployed in the suburb of Hefei ($31.9^\circ N$ $117.16^\circ E$) for the remote sensing of GHGs above rice paddies from 1 July to 15 October 2022. The atmospheric total column abundance of CO_2 , CH_4 and N_2O above rice paddies was obtained with errors of 0.7 ppm, 4 ppb and 2 ppb, respectively. Based on long-term measurement results, we found that atmospheric CO_2 concentrations were increasing, and inferred that rice paddy fields can play a role in carbon sequestration and that CH_4 and N_2O emissions from rice paddy fields are the main contributors to increasing atmospheric greenhouse gas concentrations during the rice growing season. With the advantages of portability and high accuracy, the LHRs can be used to simultaneously measure multiple GHG emissions above a large area of farmland. However, when using LHRs to detect GHG concentrations, disadvantages such as the inability to use LHRs at night and the inability to measure farmland emission fluxes limit the further application of LHRs in farmland GHG emission monitoring. The inability to monitor GHGs above rice paddy fields in

real time during thunderstorms and cloudy and rainy days greatly limited our ability to research the influence of weather on rice field emissions. In future work, we will focus on the combined use of multiple technologies, including chamber gas chromatography, the eddy covariance technique and LHRs. We would like to obtain technology to be used in high-precision flux monitoring of GHGs in small areas of farmland throughout the day under a variety of weather conditions using chamber gas chromatography and the eddy covariance technique, while the LHRs will be used for GHG concentration monitoring over large areas of farmland. Real-time monitoring of rice paddy fields' GHG emissions during the rice growing season and non-rice growing season is achieved by establishing a three-dimensional observation network. The effectiveness of various emission reduction measures will be verified. Additionally, the relationship between farmland gas emissions and farmland yield and quality will be further determined.

Author Contributions: Conceptualization, J.L. and Z.X.; methodology, J.L.; software, Y.L.; validation, Z.X., J.L., F.S. and T.T.; formal analysis, Z.X. and J.L.; investigation, Y.L.; resources, J.L.; data curation, Z.X.; writing—original draft preparation, J.L.; writing—review and editing, J.Z.; visualization, J.L. and Z.X.; supervision, G.B. and T.T.; project administration, T.T.; funding acquisition, F.S., X.G. and T.T. All authors have read and agreed to the published version of the manuscript.

Funding: This research was funded by the Key Project of the National Natural Science Foundation of China (NO. 41730103), Natural Science Foundation of Anhui Province (NO. 2208085QF218) and University Natural Science Research Program of Anhui Province (NO. 2022AH051795).

Data Availability Statement: Not applicable.

Conflicts of Interest: The authors declare no conflict of interest.

References

1. Fan, K.; Yan, Y.; Xu, D.; Li, S.; Zhao, Y.; Wang, X.; Xin, X. Methane and Nitrous Oxide Fluxes with Different Land Uses in the Temperate Meadow Steppe of Inner Mongolia, China. *Agronomy* **2022**, *12*, 2810. [CrossRef]
2. McGill, B.M.; Hamilton, S.K.; Millar, N.; Robertson, G.P. The Greenhouse Gas Cost of Agricultural Intensification with Groundwater Irrigation in a Midwest U.S. Row Cropping System. *Glob. Chang. Biol.* **2018**, *24*, 5948–5960. [CrossRef] [PubMed]
3. Duval, B.D.; Martin, J.; Marsalis, M.A. The Effect of Variable Fertilizer and Irrigation Treatments on Greenhouse Gas Fluxes from Aridland Sorghum. *Agronomy* **2022**, *12*, 3109. [CrossRef]
4. Knorr, W. Is the airborne fraction of anthropogenic CO₂ emissions increasing? *Geophys. Res. Lett.* **2009**, *36*, L21710. [CrossRef]
5. Wang, G.; Liang, Y.; Zhang, Q.; Jha, S.K.; Gao, Y.; Shen, X.; Sun, J.; Duan, A. Mitigated CH₄ and N₂O Emissions and Improved Irrigation Water Use Efficiency in Winter Wheat Field with Surface Drip Irrigation in the North China Plain. *Agric. Water Manag.* **2016**, *163*, 403–407. [CrossRef]
6. Pereira, J.L.S.; Perdigão, A.; Marques, F.; Wessel, D.F.; Trindade, H.; Fangueiro, D. Mitigating Ammonia and Greenhouse Gas Emissions from Stored Pig Slurry Using Chemical Additives and Biochars. *Agronomy* **2022**, *12*, 2744. [CrossRef]
7. IPCC. Available online: <https://www.ipcc.ch/report/sixth-assessment-report-cycle/> (accessed on 10 November 2022).
8. Zhu, X.; Burger, M.; Doane, T.A.; Horwath, W.P. Ammonia oxidation pathways and nitrifier denitrification are significant sources of N₂O and NO under low oxygen availability. *Proc. Natl. Acad. Sci. USA* **2013**, *110*, 6328–6333. [CrossRef]
9. Levy, P.; Drewer, J.; Jammet, M.; Leeson, S.; Friborg, T.; Skiba, U.; Oijen, M. Inference of spatial heterogeneity in surface fluxes from eddy covariance data: A case study from a subarctic mire ecosystem. *Agric. For. Meteorol.* **2020**, *280*, 107783. [CrossRef]
10. Gu, M.; Chen, J.; Mei, J.; Tan, T.; Wang, G.; Liu, K.; Liu, G.; Liu, X. Open-path anti-pollution multi-pass cell-based TDLAS sensor for the online measurement of atmospheric H₂O and CO₂ fluxes. *Opt. Express* **2022**, *30*, 43961–43972. [CrossRef]
11. Feng, M.Y.; Zhang, G.; Xia, L.J.; Xiong, X.; Li, B.Z.; Kong, P.; Zhan, M.J.; Zhang, Y.X. Spatial and temporal distribution of atmospheric methane in middle-low reaches of Yangtze River based on satellite observations. *Geochimica* **2021**, *50*, 121–132.
12. Wilson, E.L.; DiGregorio, A.J.; Riot, V.J.; Ammons, M.S.; Bruner, W.W.; Carter, D.; Mao, J.; Ramanathan, A.; Strahan, S.E.; Oman, L.D.; et al. A 4 U laser heterodyne radiometer for methane (CH₄) and carbon dioxide (CO₂) measurements from an occultation-viewing CubeSat. *Meas. Sci. Technol.* **2017**, *28*, 035902. [CrossRef]
13. Zenevich, S.; Gazizov, I.; Churbanov, D.; Plyashkov, Y.; Spiridonov, M.; Talipov, R.; Rodin, A. A Concept of 2U Spaceborne Multichannel Heterodyne Spectroradiometer for Greenhouse Gases Remote Sensing. *Remote Sens.* **2021**, *13*, 2235. [CrossRef]
14. Shen, F.; Wang, G.; Wang, J.; Tan, T.; Wang, G.; Jeseck, P.; Te, Y.V.; Gao, X.; Chen, W. Transportable mid-infrared laser heterodyne radiometer operating in the shot-noise dominated regime. *Opt. Lett.* **2021**, *46*, 3171. [CrossRef] [PubMed]
15. Wilson, E.L.; DiGregorio, A.J.; Villanueva, G.; Grunberg, C.E.; Souders, Z.; Miletti, K.M.; Menendez, A.; Grunberg, M.H.; Floyd, M.A.M.; Bleacher, J.E.; et al. A portable miniaturized laser heterodyne radiometer (mini-LHR) for remote measurements of column CH₄ and CO₂. *Appl. Phys. B-Lasers Opt.* **2019**, *125*, 211. [CrossRef]

16. Wang, J.; Sun, C.; Wang, G.; Zou, M.; Tan, T.; Liu, K.; Chen, W.; Gao, X. A fibered near-infrared laser heterodyne radiometer for simultaneous remote sensing of atmospheric CO₂ and CH₄. *Opt. Lasers Eng.* **2020**, *129*, 106083. [[CrossRef](#)]
17. Robinson, I.; Butcher, H.L.; Macleod, N.A.; Weidmann, D. Hollow waveguide-miniaturized quantum cascade laser heterodyne spectro-radiometer. *Opt. Express* **2021**, *29*, 2299–2308. [[CrossRef](#)] [[PubMed](#)]
18. Weidmann, D.; Perrett, B.J.; Macleod, N.A.; Jenkins, R.M. Hollow waveguide photomixing for quantum cascade laser heterodyne spectro-radiometry. *Opt. Express* **2011**, *19*, 9074–9085. [[CrossRef](#)] [[PubMed](#)]
19. Xue, Z.Y.; Shen, F.J.; Li, J.; Liu, X.H.; Wang, G.S.; Liu, K.; Gao, X.M.; Chen, W.D.; Tan, T. MEMS Modulator-Based Mid-Infrared Laser Heterodyne Radiometer for Atmospheric Remote Sensing. *Front. Phys.* **2022**, *10*, 945995. [[CrossRef](#)]
20. Xue, Z.; Shen, F.; Li, J.; Liu, X.; Wang, J.; Wang, G.; Liu, K.; Chen, W.; Gao, X.; Tan, T. A MEMS modulator-based dual-channel mid-infrared laser heterodyne radiometer for simultaneous remote sensing of atmospheric CH₄, H₂O and N₂O. *Opt. Express* **2022**, *30*, 31828–31838. [[CrossRef](#)]
21. Sun, C.; Wang, G.; Zhu, G.; Tan, T.; Liu, K.; Gao, X. Atmospheric CO₂ column concentration retrieval based on high resolution laser heterodyne spectra and evaluation method of system measuring error. *Acta Phys. Sin.* **2020**, *69*, 144201. [[CrossRef](#)]
22. Clarke, G.B.; Wilson, E.L.; Miller, J.H.; Melroy, H.R. Uncertainty analysis for the miniaturized laser heterodyne radiometer (mini-LHR) for the measurement of carbon dioxide in the atmospheric column. *Meas. Sci. Technol.* **2014**, *25*, 055204. [[CrossRef](#)]
23. Shen, F.; Wang, G.; Xue, Z.; Tan, T.; Cao, Z.; Gao, X.; Chen, W. Impact of Lock-In Time Constant on Remote Monitoring of Trace Gas in the Atmospheric Column Using Laser Heterodyne Radiometer (LHR). *Remote Sens.* **2022**, *14*, 2923. [[CrossRef](#)]
24. Weidmann, D.; Reburn, W.J.; Smith, K.M. Retrieval of atmospheric ozone profiles from an infrared quantum cascade laser heterodyne radiometer: Results and analysis. *Appl. Opt.* **2007**, *46*, 7162–7171. [[CrossRef](#)] [[PubMed](#)]
25. Dudhia, A. The reference forward model (RFM). *J. Quant. Spectrosc. Radiat. Transf.* **2017**, *186*, 243–253. [[CrossRef](#)]
26. Zou, J.; Liu, S.; Qin, Y.; Pan, G.; Zhu, D. Sewage irrigation increased methane and nitrous oxide emissions from rice paddies in southeast China. *Agric. Ecosyst. Environ.* **2009**, *129*, 516–522. [[CrossRef](#)]

Disclaimer/Publisher's Note: The statements, opinions and data contained in all publications are solely those of the individual author(s) and contributor(s) and not of MDPI and/or the editor(s). MDPI and/or the editor(s) disclaim responsibility for any injury to people or property resulting from any ideas, methods, instructions or products referred to in the content.